Geophysical Prospecting

EAGE EUROPEAN ASSOCIATION OF GEOSCIENTISTS & ENGINEERS

Geophysical Prospecting, 2013, **61** (**Suppl. 1**), 352–367 doi: 10.1111/j.1365-2478.2012.01122.x

Downhole interferometric illumination diagnosis and balancing

Joost van der Neut*

Department of Geoscience and Engineering, Delft University of Technology, Stevinweg 1, 2628 CN Delft, The Netherlands

Received May 2011, revision accepted June 2012

ABSTRACT

With seismic interferometry or the virtual source method, controlled sources can be redatumed from the Earth's surface to generate so-called virtual sources at downhole receiver locations. Generally this is done by cross-correlation of the recorded downhole data and stacking over source locations. By studying the retrieved data at zero time lag, downhole illumination conditions that determine the virtual source radiation pattern can be analysed without a velocity model. This can be beneficial for survey planning in time-lapse experiments. Moreover, the virtual source radiation pattern can be corrected by multi-dimensional deconvolution or directional balancing. Such an approach can help to improve virtual source repeatability, posing major advantages for reservoir monitoring. An algorithm is proposed for so-called illumination balancing (being closely related to directional balancing). It can be applied to single-component receiver arrays with limited aperture below a strongly heterogeneous overburden. The algorithm is demonstrated on synthetic 3D elastic data to retrieve time-lapse amplitude attributes.

Key words: Reservoir monitoring, Seismic interferometry, Virtual source.

1 INTRODUCTION

Conventional seismic imaging, characterization and monitoring rely heavily on the availability and quality of a subsurface velocity model. Especially if the shallow subsurface is strongly heterogeneous, accurate velocity models are hard to obtain, which can pose serious limitations in such environments. Bakulin and Calvert (2004) overcame this problem by placing receivers in horizontal or deviated wells below major complexities and redatuming seismic sources from their actual locations at the Earth's surface to the well by a formalism based on cross-correlation. The concept is generally referred to as the virtual source method (Bakulin and Calvert 2006) or seismic interferometry (Schuster *et al.* 2004; Schuster 2009). Since the required redatuming operators from the source level to the receiver level are actually measured, a velocity model is not required. Besides imaging below a complex overburden, the virtual source concept proved useful for a variety of applications, including reservoir monitoring (Bakulin *et al.* 2007), salt-flank imaging (Willis *et al.* 2006), sub-salt imaging (Vasconcelos, Snieder and Hornby 2008) and various others (Curtis *et al.* 2006; Schuster 2009; Ramirez and Weglein 2009; Wapenaar *et al.* 2010a; Vasconcelos, Haney and Diallo 2011).

Over the past few years seismic interferometry has evolved significantly (Wapenaar *et al.* 2010b). Besides the common correlation-based approach, several authors have used convolution (Slob and Wapenaar 2007; Poletto and Farina 2010), (single-trace) deconvolution (Vasconcelos and Snieder 2008; Poletto *et al.* 2011) and multi-dimensional deconvolution (Wapenaar *et al.* 2011). In the latter method, seismic redatuming is interpreted as an inverse problem, which can be solved in a least-squares sense. A major limitation of such an approach is that some sort of wavefield separation is required by definition, either by wavefield decomposition (Wapenaar *et al.* 2011) or time-gating (Van der Neut *et al.* 2011a). Moreover, in heterogeneous 3D media, the implementation of multi-dimensional deconvolution would ideally require 2D

*E-mail: j.r.vanderneut@tudelft.nl

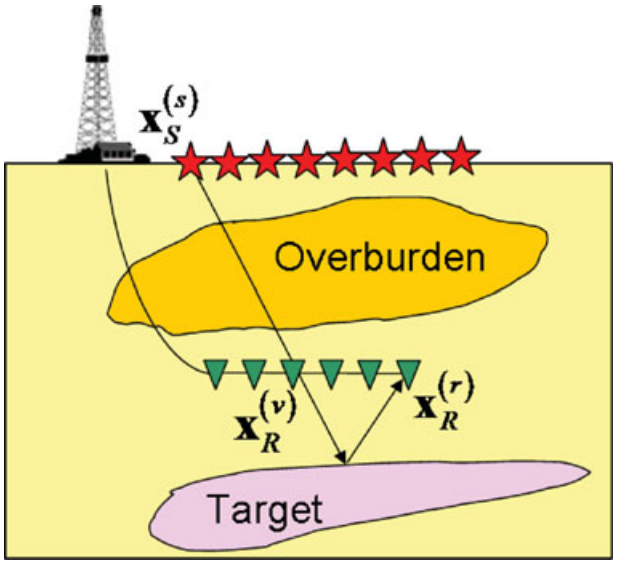

Figure 1 Configuration. Sources are redatumed from their actual locations $\mathbf{x}_S^{(s)}$ to downhole receivers $\mathbf{x}_R^{(v)}$ to bypass complexities in the overburden. A response between receivers $\mathbf{x}_R^{(v)}$ and $\mathbf{x}_R^{(r)}$ is retrieved to illuminate the target reflectors.

receiver arrays, which are not available in typical single-well acquisition.

It is well understood that interferometry by cross-correlation and multi-dimensional deconvolution are closely related through the interferometric point-spread function (Wapenaar *et al.* 2011). The point-spread function quantifies the downhole illumination conditions, which will be imprinted on the retrieved virtual source data. As such, the point-spread function can be interpreted as the radiation pattern of the virtual source and deconvolution with the point-spread function (as done in multi-dimensional deconvolution) can be seen as the optimization of this radiation pattern (Van der Neut and Bakulin 2009). In this paper, practical solutions are proposed to diagnose and optimize the radiation pattern of a virtual source in cases where acquisition conditions are limited. Implementation of the proposed algorithm will be demonstrated with a single-component receiver array of limited aperture in a horizontal borehole below a complex overburden.

2 THEORETICAL DEVELOPMENTS

The main configuration of this study is shown in Fig. 1. Sources are placed at surface locations $\mathbf{x}_S^{(s)}$. Receivers are placed in a horizontal well at locations $\mathbf{x}_R^{(r)}$. Subscripts S and R denote 'source' and 'receiver', whereas superscripts s and r are indices for the source and receiver numbers, respectively. For virtual sources, index v will be used. In the most common form of seismic interferometry (Wapenaar and Fokkema 2006), full wavefields are cross-correlated and summed over source locations, yielding the following correlation function:

$$\hat{C}\left(\mathbf{x}_R^{(r)}, \mathbf{x}_R^{(v)}, \omega\right) = \sum_s \hat{P}\left(\mathbf{x}_R^{(r)}, \mathbf{x}_S^{(s)}, \omega\right) \hat{P}^*\left(\mathbf{x}_R^{(v)}, \mathbf{x}_S^{(s)}, \omega\right) \Delta x_S. \quad (1)$$

Here, $\hat{P}(\mathbf{x}_R^{(r)}, \mathbf{x}_S^{(s)}, \omega)$ holds the recorded data from source $\mathbf{x}_S^{(s)}$ to receiver $\mathbf{x}_R^{(r)}$, ω is the angular frequency, superscript $*$ denotes complex conjugation and Δx_S is the source spacing. Equation (1) is written in the frequency-space domain, which is indicated by the caret. Various authors have shown that the causal part of the correlation function can be interpreted as an approximation of a Green's function, as if there was a source at $\mathbf{x}_R^{(v)}$ and a receiver at $\mathbf{x}_R^{(r)}$, convolved with the auto-correlated source wavelet (Bakulin and Calvert 2006; Wapenaar and Fokkema 2006). For this to be true, it is required that the source array is sufficiently extended as to sample the Fresnel zones of the reflected wavefields (Snieder 2004; Schuster 2009; Costagliola 2010) and that the source array is tapered to avoid truncation artefacts (Mehta *et al.* 2008b). Note that equation (1) is subject to a far-field radiation approximation in which amplitude-versus-rayparameter characteristics are not preserved and free-surface reflections are not accouted for (Wapenaar and Fokkema 2006; Schuster 2009).

In practice, the retrieved response by equation (1) is not always optimal and several alternative formulations have been proposed (Schuster and Zhou 2006; Snieder *et al.* 2009). In the virtual source method, for example, the full field at $\mathbf{x}_R^{(r)}$ is correlated with the time-gated direct field at $\mathbf{x}_R^{(v)}$ (Bakulin and Calvert 2006). A similar approach is taken in so-called perturbation-based interferometry (Vasconcelos, Snieder and Douma 2009) by cross-correlating the scattered field from the target reflectors at $\mathbf{x}_R^{(r)}$ with the incident field from the overburden at $\mathbf{x}_R^{(v)}$; which is

$$\hat{C}_{sc,inc}\left(\mathbf{x}_R^{(r)}, \mathbf{x}_R^{(v)}, \omega\right) = \sum_s \hat{P}_{sc}\left(\mathbf{x}_R^{(r)}, \mathbf{x}_S^{(s)}, \omega\right) \hat{P}_{inc}^*\left(\mathbf{x}_R^{(v)}, \mathbf{x}_S^{(s)}, \omega\right) \Delta x_S. \quad (2)$$

Here, subscripts *sc* and *inc* stand for 'scattered' and 'incident' constituents, respectively, which can often be separated by time-gates (Van der Neut *et al.* 2011a). The retrieved response $\hat{C}_{sc,inc}(\mathbf{x}_R^{(r)}, \mathbf{x}_R^{(v)}, \omega)$ can be interpreted as an approximation of the scattered wavefield as if there were a virtual source at $\mathbf{x}_R^{(v)}$ and a receiver at $\mathbf{x}_R^{(r)}$. The effectiveness of time-gating can be understood in several ways. Vasconcelos *et al.*

(2009) and Van der Neut *et al.* (2011a) showed that with equation (2) less spurious cross-terms are retrieved than with equation (1). Alternatively, it can be shown that time-gating improves the radiation pattern of a virtual source (Van der Neut and Bakulin 2009). Applying wavefield decomposition prior to cross-correlation proved even more successful (Mehta *et al.* 2007, 2010a). However, such decomposition requires multi-component receivers, which are often not available.

Representations for interferometry by multi-dimensional deconvolution of decomposed wavefields were derived by Wapenaar *et al.* (2011). Applications have been demonstrated for redatuming elastic wavefields below a complex overburden (Van der Neut *et al.* 2011b), virtual crosswell imaging (Minato *et al.* 2011), controlled-source electromagnetic exploration (Hunziker *et al.* 2012) and ground-penetrating radar (Slob 2009). Slight modifications have been introduced for time-gated incident and scattered wavefields (Van der Neut *et al.* 2011a). In any case, one starts with the formulation of a convolutional forward equation, which reads for time-gated wavefields:

$$\hat{P}_{sc}\left(\mathbf{x}_R^{(r)}, \mathbf{x}_S^{(s)}, \omega\right) = \sum_v \hat{X}_{sc,inc}\left(\mathbf{x}_R^{(r)}, \mathbf{x}_R^{(v)}, \omega\right)\hat{P}_{inc}\left(\mathbf{x}_R^{(v)}, \mathbf{x}_S^{(s)}, \omega\right)\Delta x_R, \tag{3}$$

where Δx_R is the receiver spacing and $\hat{X}_{sc,inc}(\mathbf{x}_R^{(r)}, \mathbf{x}_R^{(v)}, \omega)$ is a dipole impulse response as if there were an incident field emitted at $\mathbf{x}_R^{(v)}$ and a scattered field received at $\mathbf{x}_R^{(r)}$. If sufficient sources are available, equation (3) can be inverted in the least-squares sense for $\hat{X}_{sc,inc}(\mathbf{x}_R^{(r)}, \mathbf{x}_R^{(v)}, \omega)$. It can be shown that this solution obeys the following normal equation (Van der Neut *et al.* 2011a):

$$\hat{C}_{sc,inc}\left(\mathbf{x}_R^{(r)}, \mathbf{x}_S^{(w)}, \omega\right) = \sum_v \hat{X}_{sc,inc}\left(\mathbf{x}_R^{(r)}, \mathbf{x}_R^{(v)}, \omega\right) \times \hat{C}_{inc,inc}\left(\mathbf{x}_R^{(v)}, \mathbf{x}_S^{(w)}, \omega\right)\Delta x_R, \tag{4}$$

where w is another receiver index and the point-spread function is introduced as

$$\hat{C}_{inc,inc}\left(\mathbf{x}_R^{(r)}, \mathbf{x}_R^{(w)}, \omega\right) = \sum_s \hat{P}_{inc}\left(\mathbf{x}_R^{(v)}, \mathbf{x}_S^{(s)}, \omega\right) \times \hat{P}^*_{inc}\left(\mathbf{x}_R^{(w)}, \mathbf{x}_S^{(s)}, \omega\right)\Delta x_S. \tag{5}$$

The left-hand side of equation (4) is exactly the correlation function as defined in equation (2) (with index v replaced by w). The results obtained with interferometry by cross-correlation can thus be interpreted as the desired dipole impulse response $\hat{X}_{sc,inc}(\mathbf{x}_R^{(r)}, \mathbf{x}_R^{(v)}, \omega)$ blurred in time and space with the point-spread function. Given this, the point-spread function can be used to study the radiation pattern of a virtual source. Computing the point-spread function is closely related to beamforming (Lacoss 1971). It should be noted, however, that the point-spread function characterizes the illumination at a single virtual source location, whereas with beamforming one analyses the average illumination along the receiver array.

An important advantage of multi-dimensional deconvolution is that free-surface reflections are correctly handled. A deeper look into the fundamental representations of correlation-based methods shows that a homogeneous half-space above the source array should be assumed to derive equations (1) and (2) (a direct consequence of the so-called far-field radiation approximation) (Wapenaar and Fokkema 2006). For this reason, free-surface related multiples are not taken care of and can cause spurious arrivals in the retrieved responses (Van der Neut *et al.* 2011a). The representations for multi-dimensional deconvolution do not require any assumption on the medium above the sources. As multi-dimensional deconvolution changes the boundary conditions, free-surface interactions are eliminated from the retrieved responses (Wapenaar *et al.* 2011). To remove all free-surface interactions, the incident field should contain all surface-related multiples, which is often hard to achieve by time-gating (but not by wavefield decomposition).

Multi-dimensional deconvolution should not be confused with (single-)trace deconvolution as proposed by Vasconcelos and Snieder (2008). In the latter method, a reflection response $\hat{X}_{TD}(\mathbf{x}_R^{(r)}, \mathbf{x}_R^{(v)}, \omega)$ is obtained by summing deconvolution pairs, according to

$$\hat{X}_{TD}\left(\mathbf{x}_R^{(r)}, \mathbf{x}_R^{(v)}, \omega\right) = \frac{\hat{P}_{sc}\left(\mathbf{x}_R^{(r)}, \mathbf{x}_S^{(s)}, \omega\right)\hat{P}^*_{inc}\left(\mathbf{x}_R^{(v)}, \mathbf{x}_S^{(s)}, \omega\right)}{\hat{P}_{inc}\left(\mathbf{x}_R^{(v)}, \mathbf{x}_S^{(s)}, \omega\right)\hat{P}^*_{inc}\left(\mathbf{x}_R^{(v)}, \mathbf{x}_S^{(s)}, \omega\right) + \epsilon^2}, \tag{6}$$

where a small constant ϵ^2 is added for numerical stability and subscript *TD* stands for trace deconvolution. Another approach is to neglect the off-diagonal contributions in the inversion process of multi-dimensional deconvolution. This is equivalent to choosing $v = w$ in equation (4), ignoring Δx_R and removing the summation sign, yielding

$$\hat{X}_{DD}\left(\mathbf{x}_R^{(r)}, \mathbf{x}_R^{(v)}, \omega\right) = \frac{\hat{C}_{sc,inc}\left(\mathbf{x}_R^{(r)}, \mathbf{x}_R^{(v)}, \omega\right)}{\hat{C}_{inc,inc}\left(\mathbf{x}_R^{(v)}, \mathbf{x}_R^{(v)}, \omega\right) + \epsilon^2}. \tag{7}$$

Equation (7) is closely related to illumination compensation as sometimes applied in seismic migration (Nemeth, Wu and Schuster 1999), which balances the illumination strength along the receiver array. Since essentially the off-diagonal contributions in the point-spread function are neglected, this method is referred to as diagonal deconvolution, indicated by the subscript *DD*. Note that equation (6) describes a

summation over deconvolved pairs, whereas equation (7) describes a deconvolution of summed correlated pairs, which is essentially different.

3 PRACTICAL ISSUES

In practice, it is not always easy to isolate wavefields with time-gates prior to cross-correlation. However, the correlation function of full fields (equation (1)) can be interpreted as a sum of four constituents, reading in the time-space domain:

$$C\left(\mathbf{x}_R^{(r)}, \mathbf{x}_R^{(v)}, t\right) = C_{inc,inc}\left(\mathbf{x}_R^{(r)}, \mathbf{x}_R^{(v)}, t\right) + C_{sc,inc}\left(\mathbf{x}_R^{(r)}, \mathbf{x}_R^{(v)}, t\right) + C_{inc,sc}\left(\mathbf{x}_R^{(r)}, \mathbf{x}_R^{(v)}, t\right) + C_{sc,sc}\left(\mathbf{x}_R^{(r)}, \mathbf{x}_R^{(v)}, t\right). \tag{8}$$

Note that $C_{inc,inc}$ is the point-spread function (equation (5)), having its main contribution at $t = 0$ (and $v = r$). $C_{sc,inc}$ and $C_{inc,sc}$ host the scattered contributions (reflections) being located at positive and negative times, respectively. $C_{sc,sc}$ is generally weak and mostly concentrated at $t = 0$ (for $v = r$).

The constituents of C around $t = 0$ are referred to as the virtual source function, which can loosely be interpreted as the source function of the data as retrieved with interferometry by cross-correlation. The virtual source function is dominated by the point-spread function but also contains contributions from $C_{sc,sc}$. The virtual source function does not contain later arrivals from the point-spread function relating to multiples in the incident wavefield. It is assumed that the virtual source function can be isolated from the correlated data by placing a time-gate around $t = 0$. Theoretically, multi-dimensional deconvolution can be applied by deconvolving the causal contributions in C (which are dominated by $C_{sc,inc}$) by the virtual source function (approximating $C_{inc,inc}$). A similar procedure has been used before to apply multi-dimensional deconvolution on ambient noise correlations (Wapenaar *et al.* 2011). In practice, however, multi-dimensional deconvolution with time-gated fields can be difficult, especially when events are interfering and conditions for wavefield separation are not optimal. For such reasons, an alternative strategy is proposed in the following.

Consider the following $\tau - p$ transform (or slant stack) at fixed $\mathbf{x}_R^{(v)}$:

$$\breve{C}\left(p, \mathbf{x}_R^{(v)}, \tau\right) = \sum_r C\left(\mathbf{x}_R^{(r)}, \mathbf{x}_R^{(v)}, \tau + p(r - v)\Delta x_R\right)\Delta x_R. \tag{9}$$

Here, p is the rayparameter and τ is the intercept time. r and v are integers taking the values of indices r and v. In the Appendix, it is shown that if the overburden is homogeneous and the receiver array is illuminated with a maximum propagation angle of α_{max}, the $\tau - p$ transform of the correlation function converges to

$$\breve{C}\left(p, \mathbf{x}_R^{(v)}, \tau\right) = \begin{cases} \breve{S}(\tau) & \text{for} \quad p^2 \le c_a^{-2} \\ 0 & \text{for} \quad p^2 > c_a^{-2} \end{cases}. \tag{10}$$

Here, $\breve{S}(\tau)$ is the auto-spectrum of the source wavelet and $c_a = c/\sin(\alpha_{max})$ is the apparent velocity, with c being the propagation velocity. In Fig. 2(a) the time-space domain representation of such an ideal virtual source function is shown for a case with $c_a = 2000$ m/s. As expected from equation (10), the $\tau - p$ transform reveals an imprint of the source auto-spectrum $\breve{S}(\tau)$ for $-c_a^{-1} \le p \le c_a^{-1}$, see Fig. 2(b).

If the overburden is complex and / or sources are not uniformly distributed, illumination conditions can be less ideal and the virtual source function can be rayparameter-dependent within the illuminated band ($-c_a^{-1} \le p \le c_a^{-1}$). To compensate for this, a filter is introduced that balances the virtual source function at each rayparameter and virtual source location within this band, according to

$$\breve{C}'\left(p, \mathbf{x}_R^{(v)}, \tau\right) = \breve{f}\left(p, \mathbf{x}_R^{(v)}, \tau\right) * \breve{C}\left(p, \mathbf{x}_R^{(v)}, \tau\right). \tag{11}$$

Here, $\breve{C}'$ is the updated correlation function and $\breve{f}$ is a matching filter, as commonly used in adaptive subtraction (Verschuur and Berkhout 1997; Abma *et al.* 2005). To find $\breve{f}$, the following minimization problem is solved in a local window around $\tau = 0$:

$$\underset{\breve{f}}{\text{minimize}} \left|\left| \breve{D}(\tau) - \breve{f}\left(p, \mathbf{x}_R^{(v)}, \tau\right) * \breve{C}\left(p, \mathbf{x}_R^{(v)}, \tau\right) \right|\right|_2, \tag{12}$$

where subscript 2 denotes the ℓ_2-norm and $\breve{D}(\tau)$ is the desired virtual source function. An obvious choice would be $\breve{D}(\tau) = \breve{S}(\tau)$ for $-c_a^{-1} \le p \le c_a^{-1}$, such that the observed virtual source function is forced to align with the ideal virtual source function (equation (10)). An alternative route is to choose for $\breve{D}(\tau)$ a delta function $\breve{\delta}(\tau)$, which is numerically computed as a vector with zeros and one non-zero entry at $\tau = 0$. In this way the data are also temporally deconvolved by the filter and knowledge of the average source auto-spectrum is not required. The proposed approach is referred to as illumination balancing, being closely related to the directional balancing method of Curtis and Halliday (2010). In both cases the observed correlated data (C) are matched with an ideal virtual source response (D). Curtis and Halliday (2010) applied their method to full gathers in the frequency-wavenumber domain for surface-wave retrieval. Illumination balancing is applied in a local window around zero intercept time in the $\tau - p$ domain for interferometric redatuming. It was assumed that the virtual source function is flat in the $\tau - p$ domain at

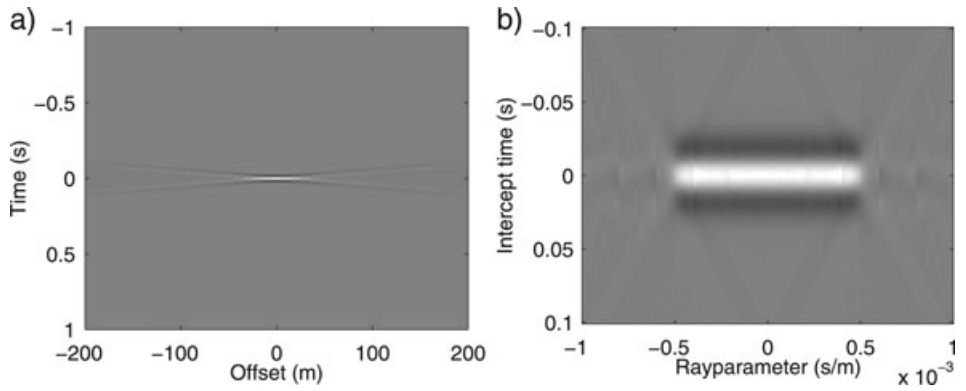

Figure 2 Virtual source function in a homogeneous medium with $c_a = 2000$ m/s in a) the time-space domain and b) the $\tau - p$ domain. The auto-spectrum of the sources is a Ricker wavelet with a peak frequency of 20 Hz.

each receiver location and $\tau = 0$. If the medium is strongly heterogeneous at the receiver level, this assumption will no longer be met. If knowledge of the local medium properties is available, this might be used for a more sophisicated estimate of $\check{D}(\tau)$.

One important practical issue that has not been addressed is dimensionality. Ideally, multi-dimensional deconvolution (or illumination balancing) requires the downhole wavefields to be sampled in two spatial directions in a 3D medium. However, the borehole samples these fields only in one spatial direction. To allow multi-dimensional deconvolution (or illumination balancing) for this configuration, a synthesized-2D solution is proposed. Directions x_1 and x_2, respectively parallel and perpendicular to the well, are distinguished. By inspection of the correlation gather in the x_2-direction, the interferometric Fresnel zones (Costagliola 2010) of the major reflections can be identified, as will be shown later. Based on this, a sub-array of sources is selected being broad in the x_1-direction and narrow in the x_2-direction but large enough to contain all relevant stationary-phase points. Correlations of all sources in the 2D sub-array are stacked to generate the correlation functions (equation (1)) to be used for multi-dimensional deconvolution or illumination balancing in the x_1-direction. As the source array is narrow in the x_2-direction, illumination variations outside the stationary-phase region that are not accounted for by the synthesized-2D assumption, are avoided to some extent.

4 RESERVOIR MONITORING EXAMPLE

Various time-lapse applications of seismic interferometry and the virtual source method have been presented in the past (Sens-Schönfelder and Wegler 2006; Bakulin *et al.* 2007; Wapenaar *et al.* 2010b). Changes in surface statics and overburden velocities are naturally compensated by cross-correlation or deconvolution (Schuster *et al.* 2004) and, as a consequence, virtual sources tend to be more repeatable than physical sources (Mehta *et al.* 2010b). Most of these studies have focused attention on the kinematics of the retrieved signals. It has been synthetically demonstrated, however, that relative amplitude-versus-rayparameter information can be retrieved with interferometry by multi-dimensional deconvolution (Van der Neut 2011). Since the scattered wavefield is deconvolved by the incident wavefield (including variations in the overburden), multi-dimensional deconvolution offers the potential to differentiate changes in the overburden from changes in the target reservoir. This is highly desirable in time-lapse processing, since changes in the shallow subsurface tend to cumulate and often mask the responses of deeper target horizons (Spetzler and Kvam 2006).

In the following, interferometric illumination diagnosis and balancing will be applied to reservoir monitoring below a complex 3D overburden. Elastic wavefields are modelled synthetically using a 3D base survey model with free surface, based on an existing oilfield in Oman (Korneev, Bakulin and Lopez 2008). In Fig. 3(a), a 2D slice (in the (x_2, x_3)-plane) of the shear-wave velocity model is shown. Horizontal vibrators are located on a 2D grid (having 141 x 39 source locations with 8 m source spacing in both directions) at the Earth's surface. All sources are polarized in the x_2-direction. At 340 m depth, a geophone array is deployed with 10 m receiver spacing, measuring particle velocity in the x_2-direction. This array is placed in a horizontal well that is oriented in the x_1-direction (perpendicular to the slice of Fig. 3a). With seismic interferometry, virtual source data will be generated as if both (virtual) sources and receivers are located in the well. Since the polarization of the vibrators is perpendicular to the receiver line in which virtual source data are retrieved, Sh-waves dominate the gathers,

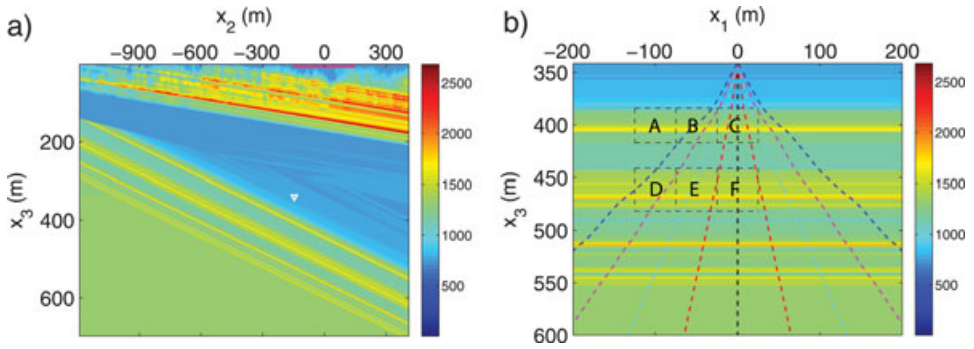

Figure 3 a) A 2D slice in the x_2-direction of the shear-wave velocity of the subsurface used for numerical modelling, in units m/s. The source array is indicated in pink. The receiver array is indicated by the white triangle. b) A 2D slice in the x_1-direction of the shear-wave velocity below the receiver array, in units m/s. The dashed black rectangles with letters A, B, C, D, E and F indicate anomalies where the medium parameters are different in the base and monitor surveys. Coloured dashed lines represent rays for a virtual source at $x_1 = 0$ m with rayparameters as provided in Table 1. x_1 and x_2 denote horizontal directions and x_3 denotes the vertical direction.

approximately obeying a scalar wave equation that can be decoupled from the system of P- and Sv-waves. In Fig. 3(b), a slice of the medium below the receivers is shown in the (x_1, x_3)-plane. After modelling the responses of the base survey, changes between 0−15% are introduced in the medium parameters (density, P- and S-wave velocity) in various parts of the reservoir, including six dashed rectangles (anomalies) that are indicated in Fig. 3(b). Medium parameters in the overburden remain unchanged. Monitor survey data are forward modelled in the evolved medium with the same source and receiver coordinates as used for modelling the base survey.

In Fig. 4(a,b), common-receiver gathers are shown for the base survey and the time-lapse response (monitor survey minus base survey), with source locations varying in the x_2-direction (at $x_1 = 0$ m). In Fig. 5(a,b) common-receiver gathers are shown with source locations varying in the x_1-direction (at $x_2 = 0$ m). It should be noted that the illuminating wavefield is strongly distorted by the complex overburden, especially in the x_1-direction (being the direction of the well). To find the stationary-phase region in the x_2-direction, auto-correlation gathers are created by auto-correlating the wavefields at the central receiver, see Fig. 6(a,b). Based on visual inspection, a subset of sources is selected, indicated by the dashed blue lines. This subset is assumed to cover the interferometric Fresnel zone of the dominant reflections (Costagliola 2010). Source tapers are applied in both the x_1- and x_2-directions to mitigate finite source aperture effects (Mehta *et al.* 2008b).

Virtual sources are generated at all 41 receiver locations using the cross-correlation of full wavefields (equation (1)). In Fig. 7(a) the retrieved response is shown at zero subsurface offset (meaning that $r = v$ at each trace). The virtual source function is removed from the retrieved gather by muting all information at $t < 0.08$ s, as indicated by the dashed red line in the figure. In Fig. 7(b) the time-lapse response is shown for all 41 virtual-source-receiver pairs at zero offset. The anomalies that are marked by dashed black rectangles in Fig. 3(b) can clearly be observed in Fig. 7(b) and are indicated by similar markers. Note that additional time-lapse responses can be found between 0.30−0.40 s. These spurious events are probably caused by travel time mismatch in the deeper section originating from the velocity changes in the shallower section (Spetzler and Kvam 2006).

5 ILLUMINATION DIAGNOSIS

As mentioned before, the retrieved virtual source data do not only contain the scattered field but also the virtual source function around $t = 0$, mainly stemming from cross-correlations of the incident field with itself. In the following, the virtual source function at a receiver location in the centre of the array ($v = 21$) will be studied carefully. First, this is done before cross-correlated traces are stacked over surface sources. In Fig. 8(a) the contribution of one particular surface source to the correlation function (including the virtual source function) is shown. This figure is obtained by cross-correlating the field observed at the virtual source location with the fields observed at all receivers for the chosen surface source. The following $\tau - pq$ transform is defined as an extension to the $\tau - p$ transform (equation (9)):

$$\breve{C}\left(p, q, \mathbf{x}_R^{(v)}, \tau\right) = \sum_r C\Big(\mathbf{x}_R^{(r)}, \mathbf{x}_R^{(v)}, \tau + p((r-v)\Delta x_R) + q((r-v)\Delta x_R)^2\Big)\Delta x_R. \quad (13)$$

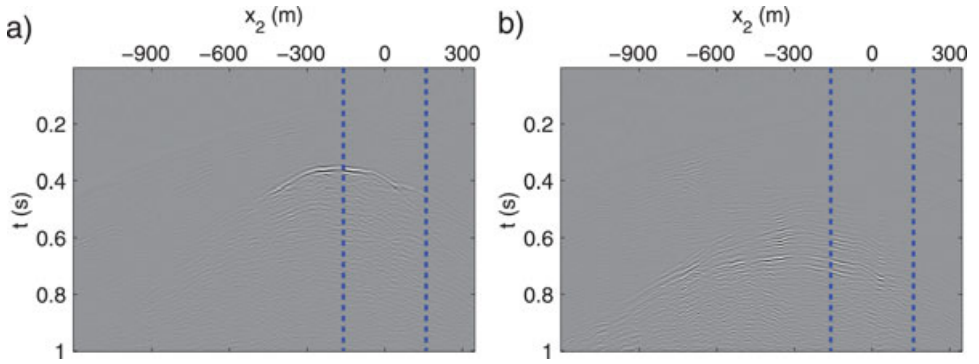

Figure 4 Common-receiver gather with source locations varying in the x_2-direction (at $x_1 = 0$ m) in the time-space domain: a) base survey, b) time-lapse response obtained by subtracting the base survey data from the monitor survey data. The dashed blue lines indicate the location of the sub-array of sources that is used for further processing.

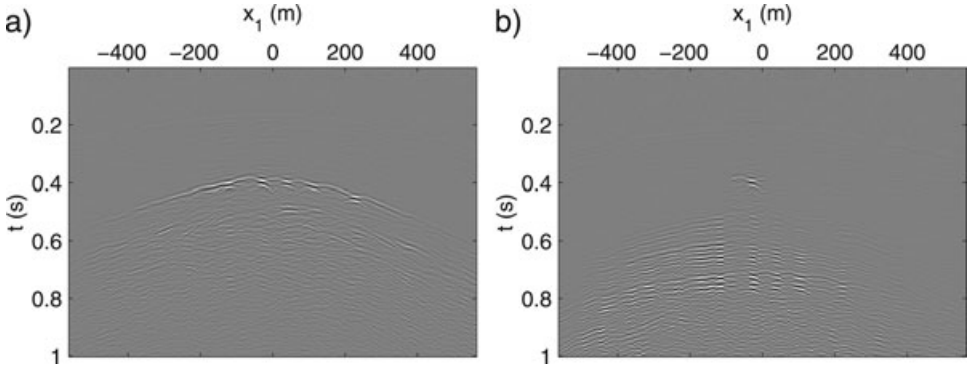

Figure 5 Common-receiver gather with source locations varying in the x_1-direction (at $x_2 = 0$ m) in the time-space domain: a) base survey, b) time-lapse response obtained by subtracting the base survey data from the monitor survey data.

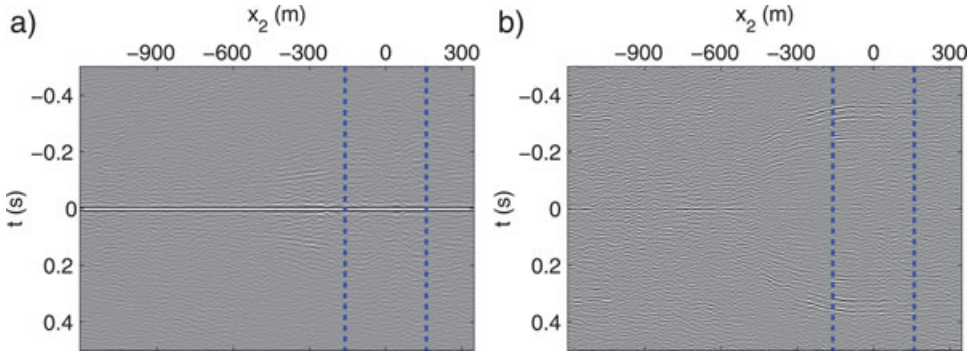

Figure 6 Auto-correlation gather in the x_2-direction (at $x_1 = 0$ m) in the time-space domain: a) base survey, b) time-lapse response obtained by subtracting the base survey data from the monitor survey data. The dashed blue lines indicate the location of the sub-array of sources that is used for further processing.

Here, q is referred to as the curvature. Taking the $\tau - pq$ transform of the correlation function at $v = 21$ and $\tau = 0$, the virtual source function can be unraveled in p and q, see Fig. 8(b). A dominant peak is found at $(p_{dom}, q_{dom}) \approx (-1.8 \cdot 10^{-4}$ s/m, $-1.1 \cdot 10^{-6}$ s/m$^2)$ where the subscript *dom* stands for dominant. To illustrate that the estimated dominant rayparameter and curvature provide a good parametrization of the event in Fig. 8(a), the function $t = p_{dom}(r\Delta x_R) + q_{dom}(r\Delta x_R)^2$ is drawn in this figure. Note that it matches the dominant event well.

Virtual source data are created by stacking cross-correlated traces over the available surface sources (equation (1)). Such

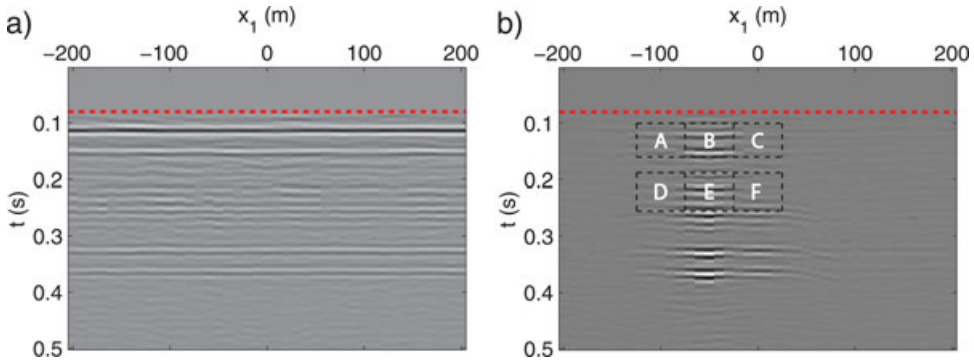

Figure 7 Zero-offset virtual-source data in the time-space domain: a) base survey, b) time-lapse response obtained by subtracting the base survey data from the monitor survey data. The virtual source function is removed by muting all data above 0.08 s (indicated by the red dashed line). The dashed black rectangles with letters A, B, C, D, E and F indicate anomalies where the medium parameters are different in the base and monitor surveys.

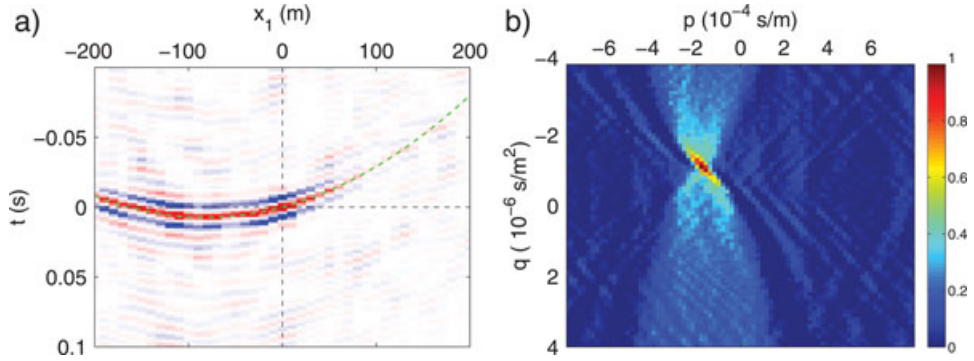

Figure 8 Correlation function for $v = 21$ from one chosen source in a) the time-space domain and b) the $\tau - pq$ domain at $\tau = 0$. The dashed green line in a) represents the function $t = p_{dom}(r\Delta x_R) + q_{dom}(r\Delta x_R)^2$, where p_{dom} and q_{dom} are the dominant rayparameter and dominant curvature extracted from b).

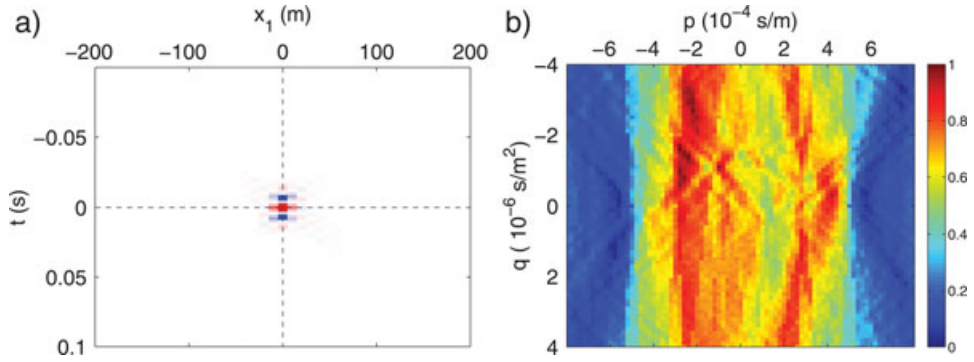

Figure 9 Correlation function for $v = 21$ after stacking sources in the x_1-direction for one chosen source line in the x_2-direction in a) the time-space domain and b) the $\tau - pq$ domain at $\tau = 0$.

a stacking process will have an effect on the retrieved virtual source function. In Fig. 9(a) the correlation function (including the virtual source function) is shown after the sources of one chosen x_2-coordinate are stacked along the x_1-direction. In Fig. 9(b), the corresponding scan over p and q is shown. A dominant orientation can no longer be observed. Note that the illuminated zone is limited in rayparameters to a band of approximately $-4 \cdot 10^{-4}$ s/m $\leq p \leq 4 \cdot 10^{-4}$ s/m. Outside this band, the virtual source was not illuminated well and, as a consequence, virtual source radiation vanishes. This

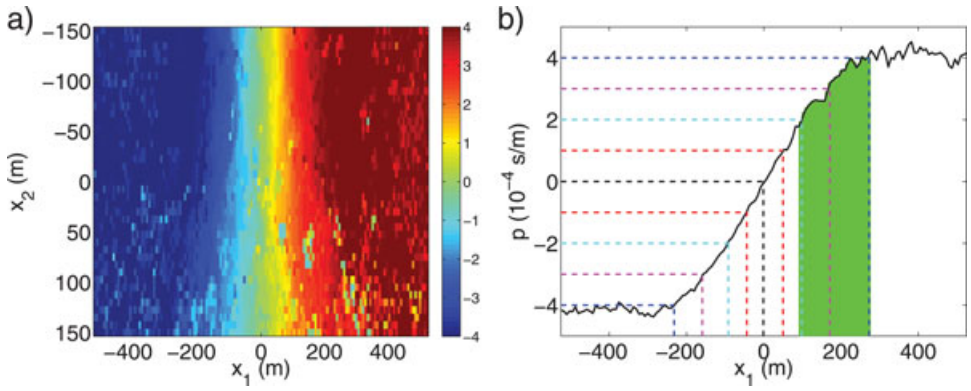

Figure 10 a) Estimated dominant rayparameter p_{dom} (in 10^{-4} s/m) of the illuminating field as a function of the source location. b) Estimated dominant rayparameter p_{dom} averaged over the source x_2-coordinate as a function of the source x_1-coordinate. Coloured dashed lines correspond to rayparameters with colour coding as provided in Table 1. The green zone indicates the source lines that are selected for the limited source array $\partial\mathbb{S}_{selected}$.

Table 1 Colour coding for the traced rays in Fig. 3(b), Fig. 10(b), and Fig. 12(a,b)

Colour	black	red	cyan	magenta	blue
$p(10^{-4}\,\mathrm{s/m})$	0	±1	±2	±3	±4

behaviour is consistent with equation (10). It can be concluded that the maximum propagation angle is approximately $\alpha_{max} = \arcsin(c_{max}^{-1}c) \approx 17.5^{\circ}$, with $c_{max}^{-1} = p_{max} = 4 \cdot 10^{-4}$ s/m and $c \approx 750$ m/s at the receiver level.

By estimating the dominant rayparameter p_{dom} of each surface source, a map can be constructed of p_{dom} as a function of the surface source location, see Fig. 10(a,b). With dashed coloured lines the different rayparameters that are provided in Table 1 are indicated. The band of illumination ($-4 \cdot 10^{-4}$ s/m $\leq p \leq 4 \cdot 10^{-4}$ s/m) can be clearly observed. The constructed map provides useful information on which source contributes to the retrieval of which rayparameter. Note that the dominant rayparameter is estimated in the x_1-direction only. For this reason, it is sensitive for the x_1-coordinate of the source but relatively insensitive for its x_2-coordinate.

Mateeva *et al.* (2007) demonstrated the advantage of steering a virtual source by selecting only those sources at the surface that contribute to the desired illumination. To achieve this, ray tracing was applied to the direct arrival in a velocity model. However, by creating a map of source-dependent illumination (Fig. 10a,b), appropriate sources can be selected without a velocity model. This is demonstrated by repeating the experiment with a smaller source array. With the help of Fig. 10(b), only the sources that radiate in the range $2 \cdot 10^{-4}$ s/m $\leq p \leq 4 \cdot 10^{-4}$ s/m are selected. These sources are indicated by the green zone in Fig. 10(b). The selected source array is referred to as $\partial\mathbb{S}_{selected}$. In Fig. 11(a) the virtual source function is shown in case sources are stacked over $\partial\mathbb{S}_{selected}$ only. Note that a preferred direction can be observed, which is even more apparent after a scan over the rayparameter and curvature, see Fig. 11(b). The imposed radiation limitation $2 \cdot 10^{-4}$ s/m $\leq p \leq 4 \cdot 10^{-4}$ s/m can well be observed. The dominant rayparameter and curvature are picked and the function $t = p_{dom}(r\Delta x_R) + q_{dom}(r\Delta x_R)^2$ is drawn in Fig. 11(a). Note that this function follows the main trend in the virtual source function well.

In Fig. 12(a,b) the retrieved time-lapse responses are shown using all sources and only sources in $\partial\mathbb{S}_{selected}$, respectively. Rays are traced in the gathers with rayparameters as indicated in Table 1. Note that in Fig. 12(b) only anomalies in the green zone (corresponding to the selected rayparameters $2 \cdot 10^{-4}$ s/m $\leq p \leq 4 \cdot 10^{-4}$ s/m) are detected. This is a consequence of limiting the illumination from the surface and, consequently, limiting the virtual source radiation direction.

Through a survey with a sparse but wide source grid, the general dominant rayparameter might be mapped as a function of source location (as in Fig. 10a). With the help of such an illumination map, denser source arrays can be designed to steer the virtual source in the direction of interest. Alternatively, in time-lapse experiments, a base survey can be conducted with a wide grid of sources and, depending on the target of interest, a smaller sub-grid can be selected for monitoring. When the imaging target is more complex, as for instance in salt-flank and sub-salt imaging (Willis *et al.* 2006; Mateeva *et al.* 2007; Vasconcelos *et al.* 2008),

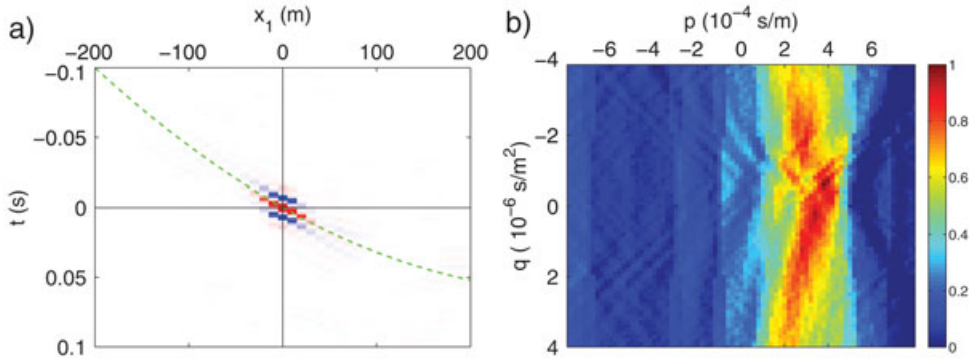

Figure 11 Correlation function for $v = 21$ after stacking only over sources within $\partial\mathbb{S}_{selected}$ (indicated in green in Fig. 10b) in the x_1-direction for one chosen source line in the x_2-direction in a) the time-space domain and b) the $\tau - pq$ domain at $\tau = 0$. The dashed green line in a) represents the function $t = p_{dom}(r\Delta x_R) + q_{dom}(r\Delta x_R)^2$, where p_{dom} and q_{dom} are the dominant rayparameter and dominant curvature extracted from b).

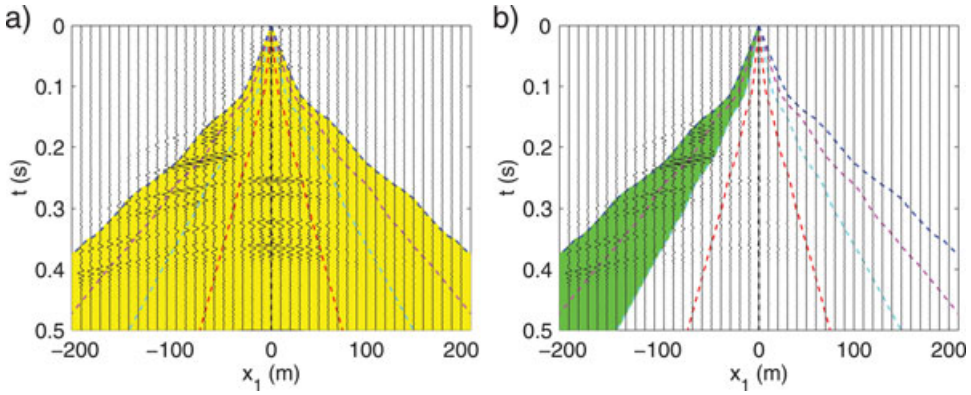

Figure 12 Retrieved time-lapse response of a virtual source at $v = 21$ after stacking a) all sources and b) only sources within $\partial\mathbb{S}_{selected}$ (indicated in green in Fig. 10b). Coloured dashed lines are rays with colour coding as provided in Table 1. The yellow and green zones represent the illuminated portions of the gathers using all sources and only sources within $\partial\mathbb{S}_{selected}$, respectively.

steered virtual-source radiation may also simplify the interpretation of the retrieved records considerably.

6 ILLUMINATION BALANCING

Mehta *et al.* (2010b) discussed two problems that can hamper reservoir monitoring with downhole receivers: 1) non-repeatable source coupling and 2) obstructions of the source array (i.e., missing sources). Concerning non-repeatable source coupling, a distinction can be made between the emitted phase and amplitude spectra. When creating virtual source data with equations (1) or (2), cross-correlation naturally compensates for non-repeatability of the phase spectra. However, non-repeatability of the amplitude spectra and missing sources are not accounted for by the correlation-based theory. Illumination balancing is one possible way to improve the retrieved signals, as will be demonstrated with an example.

In Fig. 13(a), a map is shown of the surface source array. The source coupling is assumed to be similar in the base and monitor surveys, except for zone X that is indicated in grey. In this zone, high frequencies were relatively more attenuated, as shown in Fig. 13(b). The sources were scaled such that the frequency-integrated autospectrum $\int \hat{S}(\omega)d\omega$ of the base survey is equal to that of the monitor survey at each source location in the survey. Apart from the source coupling issues in zone X, there is an obstruction in the source array (i.e., missing sources) of the monitor survey, indicated as zone Y in Fig. 13(a).

After cross-correlation and stacking (equation (1)), the retrieved data are re-sorted with respect to downhole common midpoint locations. At each common midpoint location, the correlation function is transformed to the $\tau - p$ domain and evaluated at $\tau = 0$ to analyse the virtual source function. In the upper panel of Fig. 14(a) the virtual source functions of the base and monitor surveys are shown at common midpoint

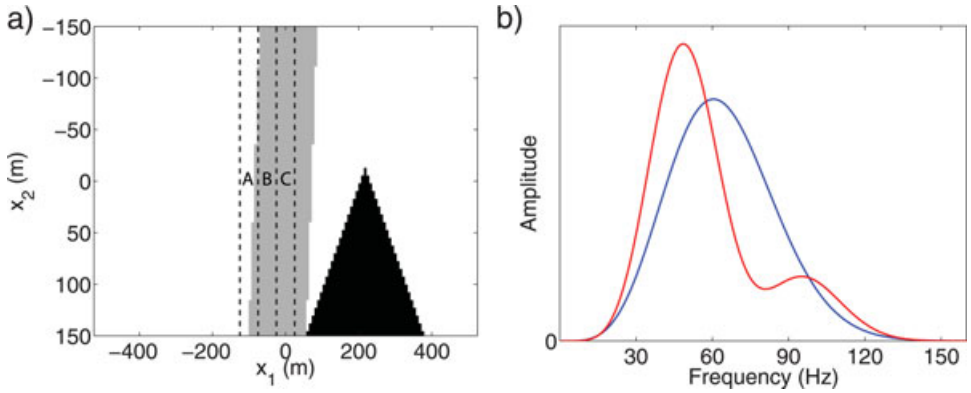

Figure 13 Map of the source array, showing the location of the anomalies with dashed black lines. Zone X (in grey) depicts sources that have different coupling conditions in the monitor survey. Zone Y (in black) depicts sources that are missing in the monitor survey. b) Source spectra of the distorted sources in zone X in the monitor survey (in red) and of all other sources in the base and monitor surveys (in blue).

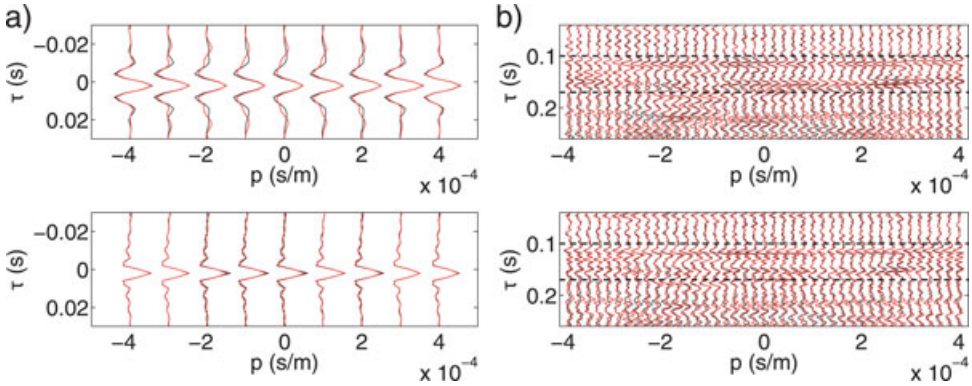

Figure 14 a) Virtual source function in the $\tau - p$ domain at common midpoint location $x_1 = -50$ m before (upper panel) and after (lower panel) illumination balancing. Every fifth trace is shown. b) Retrieved reflections in the $\tau - p$ domain at common midpoint location $x_1 = -50$ m before (upper panel) and after (lower panel) illumination balancing. Every trace is shown. The time-gate that is used to retrieve the signals in Figs. 15–17 is indicated by a black dashed line. In all figures the signals from the base and monitor surveys are shown in black and red, respectively.

location $x_2 = -50$ m, being situated right above the centre of anomaly B (see Fig. 3b). Note that the virtual source functions of the base and monitor surveys at this common midpoint location are different in terms of frequency content, especially near $p = 0$ s/m. This is caused by the non-repeatable sources in zone X (Fig. 13b), crossing this common midpoint location at the surface (Fig. 13a). Using equation (12), the virtual source functions of both surveys are matched to a desired function $D(\tau)$ (in this case a delta function) at each common midpoint location and rayparameter. The virtual source functions after matching are shown in the lower panel of Fig. 14(a). Note that the mismatch in frequency content has largely been suppressed. Illumination balancing is implemented by applying the obtained matching filters to the reflected fields at each common midpoint location and rayparameter. Results of this operation are shown in Fig. 14(b).

Before analysing the reflected signals in more detail, the change in the virtual source function's peak amplitude is studied at each common midpoint location and rayparameter. This is done by subtracting virtual source function peak amplitudes of the monitor and base surveys and normalizing with the peak amplitude of the base survey. The resulting map is shown in Fig. 15(a). The imprint from zone Y can clearly be observed at high x_1 and high p. Recall that in zone X the frequency-integrated auto-spectra $\int \hat{S}(\omega)d\omega$ of the base and monitor surveys are similar at each source location. Therefore the contributions from this zone to the virtual source function's peak amplitude of the base and monitor surveys are almost similar, such that no imprint can be observed in Fig. 15(a).

The relative change in reflected amplitudes from the upper anomalies (indicated by A, B and C in Fig. 3b) is estimated.

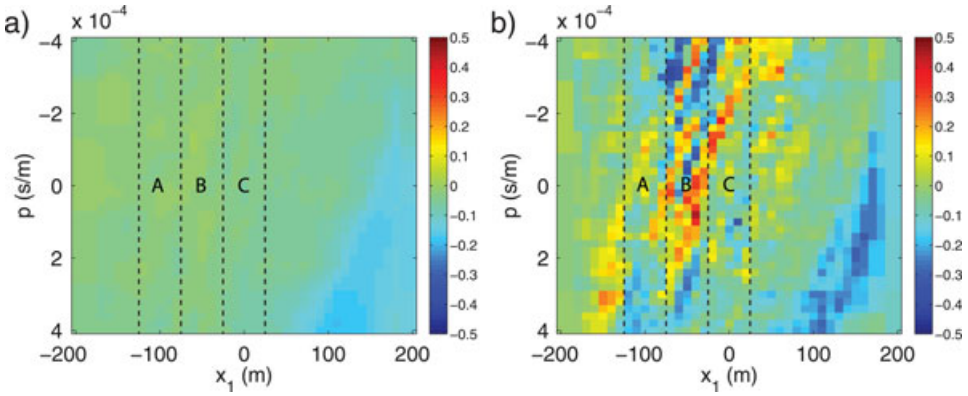

Figure 15 a) Change of the virtual source function's peak amplitudes at each common midpoint location x_1 and rayparameter p. b) Retrieved change of reflected amplitudes in the upper zone of the virtual source data ($0.10\,\text{s} \leq t \leq 0.17\,\text{s}$) at each common midpoint location x_1 and rayparameter p before illumination balancing. The locations of anomalies A, B and C are indicated.

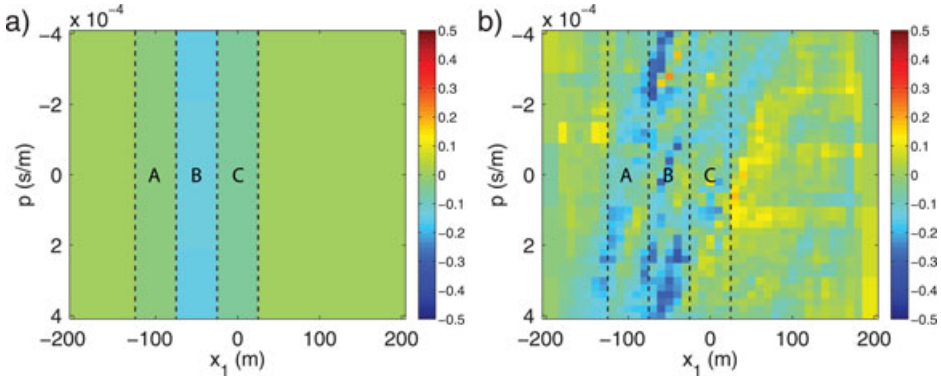

Figure 16 Expected change of reflected amplitudes in the upper zone of the virtual source data ($0.10\,\text{s} \leq t \leq 0.17\,\text{s}$) at each common midpoint location x_1 and rayparameter p. b) Retrieved change of reflected amplitudes in the upper zone of the virtual source data ($0.10\,\text{s} \leq t \leq 0.17\,\text{s}$) at each common midpoint location x_1 and rayparameter p after illumination balancing. The locations of anomalies A, B and C are indicated.

The reflections in the upper zone ($0.10\,\text{s} \leq \tau \leq 0.17\,\text{s}$) that contain these anomalies are time-gated in the common midpoint gathers. The time-gate is indicated in Fig. 14(b). The amplitude spectrum of each time-gated trace is summed over all frequencies to estimate the total reflected amplitude in that trace. The change in reflected amplitudes is computed by taking the difference of the monitor and base surveys and normalizing with the base survey. In Fig. 15(b), the estimated change of the reflected amplitude is shown before illumination balancing was applied. A reference response is computed by generating amplitude-versus-rayparameter curves using Shuey's approximation (Shuey 1985) at each common midpoint location, using contrasts as estimated from the velocity and density models; see Fig. 16(a). By comparing Fig. 15(b) and Fig. 16(a), it is observed that the retrieved amplitude change without illumination balancing is masked by 1) an imprint from zone X masking the target anomalies and 2) an imprint from zone Y giving the impression of a second anomaly at high x_1 and high p. Note the correlation of the fake second anomaly caused by zone Y with the change of the virtual source function's peak amplitude observed in Fig. 15(a). The change of reflectivity after illumination balancing is shown in Fig. 16(b). As intended, the imprints from zones X and Y were attenuated by illumination balancing and the underlying anomalies are better exposed.

In theory, exact amplitude-versus-rayparameter curves can be retrieved with interferometry, which can be inverted for the amplitude-versus-rayparameter intercept and gradient, as demonstrated for a simple synthetic model by Van der Neut (2011). However, with few single-component downhole receivers in complex 3D media, the retrieval of true-amplitude signals is hard in practice. In Fig. 17(a), the amplitude-versus-rayparameter curve of anomaly B (see Fig. 3b) is shown after averaging over common midpoint locations $-75\,\text{m} \leq x_1 \leq -25\,\text{m}$. Note that even after illumination balancing and averaging, the retrieved amplitude-versus-rayparameter

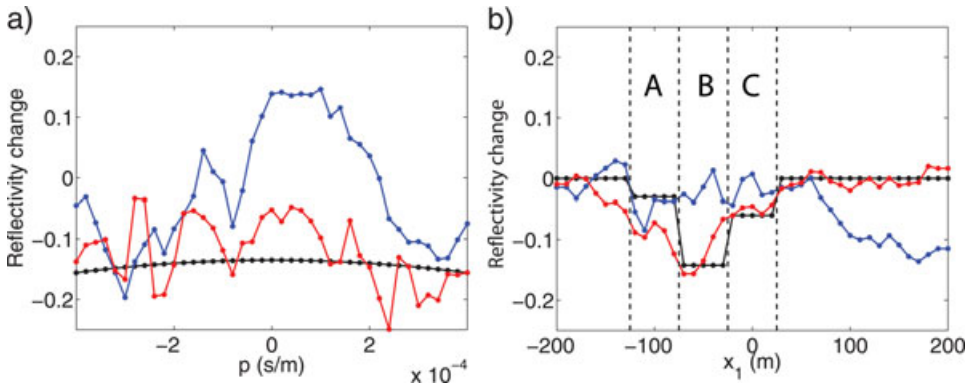

Figure 17 a) Retrieved amplitude-versus-rayparameter curves of anomaly B after averaging over common midpoint locations $-75\,\text{m} \leq x_1 \leq -25\,\text{m}$. b) Retrieved reflectivity change averaged over rayparameters. The locations of anomalies A, B and C are indicated by dashed black lines. The blue and red curves are extracted without and with illumination balancing, respectively. The black curves are computed from the model.

response is still noisy. Although retrieving the amplitude-versus-rayparameter gradient might be difficult, the amplitude-versus-rayparameter intercept can be estimated relatively well. To demonstrate this, the retrieved change of reflectivity is averaged over rayparameters (neglecting rayparameter dependence) at each common midpoint location. Results are shown in Fig. 17(b). Note that without illumination balancing the target anomaly is obstructed by the imprints from zone X, whereas the fake second anomaly caused by the missing sources in zone Y can be misleading for interpretation. Implementation of illumination balancing has resulted in improved localization and characterization of the anomaly, although the reflectivity change in anomaly A is slightly overestimated. By combining the observed changes in reflectivity with time-shift information, for instance from virtual refraction data (Tatanova, Mehta and Kashtan 2011), an inversion for the change of medium parameters might be possible.

7 DISCUSSION

In the previous example, non-repeatability at the source side was addressed. However, multi-dimensional deconvolution or illumination balancing might also be used to eliminate the effects of changes in the overburden. It is noticed that illumination balancing is closely related to the self-decon method of Mehta *et al.* (2008a), where the source spectra are deconvolved in the correlation gathers prior to source summation. Note that Mehta *et al.* (2008a) applied deconvolution at each source location, similar to equation (6), whereas illumination balancing is derived from equation (4) and involves deconvolution at each rayparameter after source summation. Illumination balancing can also be used to remove the imprints of missing sources, which is not possible with the self-decon method. An alternative way to deal with the missing sources is interpolation in the correlation gather, as suggested by Poliannikov and Willis (2011).

In this study, a Ricker wavelet was used for the source function. In realistic scenarios, the source function will generally be more complex and an initial deconvolution step might have to be applied prior to interferometry to be able to differentiate the virtual source function from the reflected signals (Poletto, Corubolo and Comelli 2010). A relatively tight source spacing of 8 m was used in the synthetic example to prevent aliasing of S-waves. For P-waves generated by vertical vibrators, larger source intervals can probably be tolerated. 3D effects remain challenging in the application of multi-dimensional deconvolution or illumination balancing. Under the current implementation, synthesized-2D data are created by stacking over a number of source lines in the x_2-direction (perpendicular to the receiver array). Constructive interference is assumed at the stationary points and destructive interference elsewhere in the gather. To further eliminate contributions outside the interferometric Fresnel zones, velocity filtering or SVD-based filtering (as proposed by Melo *et al.* 2010) might be applied to the correlation gathers in the x_2-direction prior to source-line summation.

Illumination balancing is applied after $\tau - p$ transformation of the correlation function. Instead, interferometric redatuming itself can be applied in the $\tau - p$ domain (Tao 2011) and illumination balancing can follow. Similar concepts may also be applied in passive seismic interferometry. Draganov *et al.* (2009) showed how a reflection response of the Earth's subsurface can be retrieved by cross-correlation of ambient seismic noise records. The success of this method strongly depends on the distribution of subsurface noise sources. Instead of cross-correlating long records of seismic noise, virtual

source data can also be retrieved by selecting events in passive records and cross-correlating these separately. This is the approach taken in event-driven passive seismic interferometry (Draganov *et al.* 2010). Each passive source gives a contribution to the virtual source function. By studying these individual contributions, a virtual source can be manufactured that radiates uniformly within a certain range of rayparameters. A comparable route was taken for lithospheric scale imaging by Ruigrok *et al.* (2010). Almagro Vidal *et al.* (2011) showed that analysis of the virtual source function can also be used to distinguish surface waves from body waves in correlated panels of passive data. If passive source distributions are limited, virtual source radiation will be limited accordingly. Studying the virtual source function can reveal such limitations. Illumination balancing in the $\tau - p$ domain might be a robust way to remove the directivity imprint of passive sources from retrieved reflection data.

8 CONCLUSION

Traditionally, seismic interferometry has been applied by cross-correlation. From a theoretical standpoint it is better to replace cross-correlation by an inversion process, referred to as multi-dimensional deconvolution. This process can be interpreted as optimizing the radiation pattern of a virtual source at a receiver location. Although the advantages of such an approach have been demonstrated before, implementation can be difficult, since some type of wavefield separation (either by decomposition or time-gating) has to be applied prior to inversion. If wavefield separation is not an option, the virtual source radiation pattern can still be analysed by studying the cross-correlations of full wavefields at zero time lag. By illumination balancing, the directivity in the radiation pattern can be reduced. This is especially interesting for reservoir monitoring, since the process allows us to remove non-repeatability in the illuminating source fields from the desired time-lapse response. In theory, correct amplitude-versus-rayparameter information can be retrieved by accurate interferometric redatuming. In practice, achieving this is difficult in cases with limited 1D downhole receiver arrays below a complex 3D overburden.

ACKNOWLEDGEMENTS

This research is supported by the Dutch Technology Foundation STW, applied science division of NWO and the Dutch Technology Program of the Ministry of Economic Affairs. I thank Shell E&P for providing the elastic model used in this study. I am thankful to Kees Wapenaar, Elmer Ruigrok (Delft University of Technology), Maria Tatanova, Kurang Mehta and Jorge Lopez (Shell E&P) for stimulating discussions.

REFERENCES

Abma R., Kabir N., Matson K.H., Michell S., Shaw S.A. and McLain B. 2005. Comparisons of adaptive subtraction methods for multiple attenuation. *The Leading Edge* **24**, 277–280.

Almagro Vidal C., Van der Neut J., Draganov D., Drijkoningen G. and Wapenaar K. 2011. Retrieval of reflections from ambient-noise field data using illumination diagnostics. *81st Annual Meeting, SEG, Expanded Abstracts* pp. 1613–1617.

Bakulin A. and Calvert R. 2004. Virtual source: new method for imaging and 4d below complex overburden. *74th Annual Meeting, SEG, Expanded Abstracts* pp. 2477–2480.

Bakulin A. and Calvert R. 2006. The virtual source method: Theory and case study. *Geophysics* **71**, SI139–SI150.

Bakulin A., Mateeva A., Mehta K., Jorgensen P., Ferrandis J., Sinha Herhold I. and Lopez J. 2007. Virtual source applications to imaging and reservoir monitoring. *The Leading Edge* **26**, 732–740.

Costagliola S. 2010. The interferometric fresnel zone. *72nd EAGE Conference and Exhibition, Expanded Abstracts* p. P403.

Curtis A. and Halliday D. 2010. Directional balancing for seismic and general wavefield interferometry. *Geophysics* **75**, SA1–SA14.

Curtis A., Gerstoft P., Sato H., Snieder R. and Wapenaar K. 2006. Seismic interferometry - turning noise into signal. *The Leading Edge* **25**, 1082–1092.

Draganov D., Campman X., Thorbecke J., Verdel A. and Wapenaar K. 2009. Reflection images from ambient seismic noise. *Geophysics* **74**, A63–A67.

Draganov D., Campman X., Thorbecke J., Verdel A. and Wapenaar K. 2010. Event-driven seismic interferometry with ambient seismic noise. *72nd EAGE Conference and Exhibition, Expanded Abstracts* p. G013.

*Hunziker J., Slob E., Fan Y., Snieder R. and Wapenaar K. 2012. Two-dimensional controlled-source electromagnetic interferometry by multidimensional deconvolution: spatial sampling aspects. *Geophysical Prospecting* **60**, 974–994.

Korneev V., Bakulin A. and Lopez J. 2008. Imaging and monitoring with virtual sources on a synthetic 3d data set from the middle east. *78th Annual Meeting, SEG, Expanded Abstracts*, pp. 3204–3208.

Lacoss R.T. 1971. Data adaptive spectral analysis methods. *Geophysics* **36**, 661–675.

Mateeva A., Ferrandis J., Bakulin A., Jorgensen P., Gentry C. and Lopez J. 2007. Steering virtual sources for salt and subsalt imaging. *77th Annual Meeting, SEG, Expanded Abstracts* pp. 3044–3048.

Mehta K., Bakulin A., Sheiman J., Calvert R. and Snieder R. 2007. Improving the virtual source method by wavefield separation. *Geophysics* **72**, V79–V86.

Mehta K., Sheiman J.L., Snieder R. and Calvert R. 2008. Strenghtening the virtual-source method for time-lapse monitoring. *Geophysics* **73**, S73–S80.

Mehta K., Snieder R., Calvert R. and Sheiman J. 2008. Acquisition geometry requirements for generating virtual-source data. *The Leading Edge* **27**, 620–629.

Mehta K., Kiyashchenko D., Jorgensen P., Lopez J., Ferrandis J., and Costello M. 2010. Virtual source method applied to cross-well and horizontal well geometries. *The Leading Edge* **29**, 712–723.

Mehta K., Lopez J., Matheny P. and Rocco G. 2010. Robustness of virtual source surveys in horizontal wells for reservoir monitoring in south oman. *80th Annual Meeting, SEG, Expanded Abstracts*, pp. 4185–4189.

Melo G., Malcolm A., Mikessel D. and Van Wijk K. 2010. Using svd for improved interferometric green's function recovery. *80th Annual Meeting, SEG, Expanded Abstracts*, pp. 3986–3990.

Minato S., Matsuoka T., Tsuji T., Draganov D., Hunziker J. and Wapenaar K. 2011. Seismic interferometry using multidimensional deconvolution and crosscorrelation for crosswell seismic reflection data without borehole sources. *Geophysics* **76**, SA19–SA34.

Nemeth T., Wu C. and Schuster G.T. 1999. Least-squares migration of incomplete reflection data. *Geophysics* **64**, 208–221.

Poletto F. and Farina B. 2010. Synthetisis and composition of virtual-reflector (vr) signals. *Geophysics* **75**, SA45–SA59.

Poletto F., Corubolo P. and Comelli P. 2010. Drill-bit seismic interferometry with and without pilot signals. *Geophysical Prospecting* **58**, 257–265.

Poletto F., Petronio L., Farina B. and Schleifer A. 2011. Seismic interferometry experiment in a shallow cased borehole using a seismic vibrator source. *Geophysical Prospecting* **59**, 464–476.

Poliannikov O.V. and Willis M.E. 2011. Interferometric correlogram-space analysis. *Geophysics* **76**, SA9–SA17.

Ramirez A.C. and Weglein A.B. 2009. Green's theorem as a comprehensive framework for data reconstruction, regularization, wavefield separation, seismic interferometry, and wavelet estimation: a tutorial. *Geophysics* **74**, W35–W62.

Ruigrok E., Campman X., Draganov D. and Wapenaar K. 2010. High-resolution lithospheric imaging with seismic interferometry. *Geophysical Journal International* **183**, 339–357.

Schuster G. 2009. *Seismic Interferometry*, Cambridge University Press.

Schuster G.T. and Zhou M. 2006. A theoretical overview of model-based and correlation-based redatuming methods. *Geophysics* **71**, SI103–SI110.

Schuster G.T., Yu J., Sheng J. and Rickett J. 2004. Interferometric/daylight seismic imaging. *Geophysical Journal International* **157**, 838–852.

Sens-Schönfelder C. and Wegler U. 2006. Passive image interferometry and seasonal variations of seismic velocities at merapi volcano, indonesia. *Geophysical Research Letters* **33**, L21302.

Shuey R.T. 1985. A simplification of the zoeppritz equations. *Geophysics* **50**, 609–614.

Slob E. 2009. Interferometry by deconvolution of multicomponent multioffset gpr data. *IEEE Transactions on Geoscience and Remote Sensing* **47**, 828–838.

Slob E. and Wapenaar K. 2007. Gpr without a source: cross-correlation and cross-convolution methods. *IEEE Transactions on Geoscience and Remote Sensing* **45**, 2501–2510.

Snieder R. 2004. Extracting the green's function from the correlation of coda waves: a derivation based on stationary phase. *Physical Review E* **69**, 046610.

Snieder R., Miyazawa M., Slob E., Vasconcelos I. and Wapenaar K. 2009. A comparison of strategies for seismic interferometry. *Surveys in Geophysics* **30**, 503–523.

Spetzler J. and Kvam Ø. 2006. Discrimination between phase and amplitude attributes in time-lapse seismic streamer data. *Geophysics* **71**, O9–O19.

Tao Y. 2011. Seismic interferometry in the plane-wave domain. *81st Annual Meeting, SEG, Expanded Abstracts*, pp. 3424–3829.

Tatanova M., Mehta K. and Kashtan B. 2011. Virtual refraction tomography: application to realistic 3d model. *81st Annual Meeting, SEG, Expanded Abstracts*, pp. 4239–4243.

Van der Neut J. 2011. True amplitude interferometric redatuming by multi-dimensional deconvolution and applications for reservoir monitoring, *81st Annual Meeting, SEG, Expanded Abstracts* pp. 3793–3798.

Van der Neut J. and Bakulin A. 2009. Estimating and correcting the amplitude radiation pattern of a virtual source. *Geophysics* **74**, SI27–SI36.

Van der Neut J., Tatanova M., Thorbecke J., Slob E. and Wapenaar K. 2011. Deghosting, demultiple and deblurring in controlled-source seismic interferometry. *International Journal of Geophysics* **2011**, 870819.

Van der Neut J., Thorbecke J., Mehta K., Slob E. and Wapenaar K. 2011. Controlled-source interferometric redatuming by cross-correlation and multidimensional deconvolution in elastic media. *Geophysics* **76**, SA63–SA76.

Vasconcelos I. and Snieder R. 2008. Interferometry by deconvolution, part 1: theory for acoustic waves and numerical examples. *Geophysics* **73**, S115–S128.

Vasconcelos I., Snieder R. and Hornby B. 2008. Imaging internal multiples from subsalt vsp data - examples of target-oriented interferometry. *Geophysics* **73**, S157–S168.

Vasconcelos I., Snieder R. and Douma H. 2009. Representation theorems and green's function retrieval for scattering in acoustic media. *Physical Review E* **80**, 036605.

Vasconcelos I., Haney M. and Diallo M.S. 2011. Introduction to this special section: interferometry applications. *The Leading Edge* **30**, 502–504.

Verschuur D.J. and Berkhout A.J. 1997. Estimation of multiple scattering by iterative inversion, part ii: practical aspects and examples. *Geophysics* **62**, 1595–1611.

*Wapenaar K. and Fokkema J. 2006. Green's function representations for seismic interferometry. *Geophysics* **71**, SI33–SI46.

Wapenaar K., Draganov D., Snieder R., Campman X. and Verdel A. 2010. Tutorial on seismic interferometry: part 1 - basic principles and applications. *Geophysics* **75**, 75A195–75A209.

Wapenaar K., Slob E., Snieder R. and Curtis A. 2010. Tutorial on seismic interferometry: part 2 - underlying theory and new advances. *Geophysics* **75**, 75A211–75A227.

Wapenaar K., Van der Neut J., Ruigrok E., Draganov D., Hunziker J., Slob E., Thorbecke J. and Snieder R. 2011. Seismic interferometry by crosscorrelation and by multidimensional deconvolution: a systematic comparison. *Geophysical Journal International* **185**, 1335–1364.

Willis M.E., Lu R., Campman X., Toksöz M.N., Zhang Y. and de Hoop M.V. 2006. A novel application of time-reverse acoustics: salt-dome flank imaging using walkaway vsp surveys. *Geophysics* **71**, A7–A11.

APPENDIX: THE CORRELATION FUNCTION IN A HOMOGENEOUS MEDIUM

Consider a horizontal source array of finite aperture at a distance Z above a horizontal receiver array of infinite aperture. Source and receiver spacings are equal. A reference virtual source is generated in the centre of the receiver array, which is illuminated with a maximum angle α_{max}. Since a homogeneous medium is shift-invariant, the correlation function at the reference virtual source can be expressed as

$$\hat{C}(x^{(r)}, \omega) = \sum_s \hat{P}(x^{(r)} - x^{(s)}, \omega)\hat{P}^*(-x^{(s)}, \omega)\Delta x_S. \tag{A1}$$

Here, $\hat{P}(x^{(r)}, \omega)$ is a shot record from a source that is located directly above the virtual source location. Equation (A1) can be transformed to the frequency-wavenumber domain, for which the following discrete $f-k$ transform is introduced:

$$\tilde{C}(k, \omega) = \sum_r \hat{C}(x^{(r)}, \omega) \exp(jkx^{(r)})\Delta x_R, \tag{A2}$$

where j is the imaginary unit and k is the horizontal wavenumber. Applying the $f-k$ transformation to equation (A1) yields the following (for $\Delta x_R = \Delta x_S$):

$$\tilde{C}(k, \omega) = \tilde{P}(k, \omega)\tilde{P}^*(k, \omega). \tag{A3}$$

When dipole sources are deployed (for instance vertically oriented vibrators at the free surface), the incident field can be expressed as (Wapenaar *et al.* 2011):

$$\tilde{P}(k, \omega) = \hat{s}(\omega) \times \begin{cases} \exp\left(-j\,\mathrm{sgn}(\omega)\sqrt{\omega^2 c_a^{-2} - k^2}\,Z\right) & \text{for} \quad k^2 \le \omega^2 c_a^{-2} \\ \exp\left(-\sqrt{k^2 - \omega^2 c_a^{-2}}\,Z\right) & \text{for} \quad k^2 > \omega^2 c_a^{-2} \end{cases} \tag{A4}$$

where $c_a = c/\sin\alpha_{max}$, c is the propagation velocity and $\hat{s}(\omega)$ is the spectrum of the source wavelet. Substitution of equation (A4) into (A3) yields

$$\tilde{C}(k, \omega) = \hat{S}(\omega) \times \begin{cases} 1 & \text{for} \quad k^2 \le \omega^2 c_a^{-2} \\ \exp\left(-2\sqrt{k^2 - \omega^2 c_a^{-2}}\,Z\right) & \text{for} \quad k^2 > \omega^2 c_a^{-2} \end{cases} \tag{A5}$$

Here, $\hat{S}(\omega) = |\hat{s}(\omega)|^2$ is the source auto-spectrum. The $\tau - p$ transform as introduced in equation (9) can be expressed for the shift-invariant medium as

$$\breve{C}(p, \tau) = \sum_r C(x^{(r)}, \tau + px^{(r)})\Delta x_R. \tag{A6}$$

By applying the forward temporal Fourier transformation to equation (A6) and using the shift property, it follows that

$$\int_{-\infty}^{+\infty} \breve{C}(p, \tau) \exp(j\omega\tau)d\tau = \sum_r \hat{C}(x^{(r)}, \omega) \exp(j\omega px^{(r)})\Delta x_R. \tag{A7}$$

By taking $k = \omega p$, the right-hand side of equations (A7) and (A2) are identical. It follows that the left-hand side of equation (A7) is equal to $\tilde{C}(k, \omega)$, which is given by equation (A5) and consequently

$$\int_{-\infty}^{+\infty} \breve{C}(p, \tau) \exp(j\omega\tau)d\tau = \hat{S}(\omega) \times \begin{cases} 1 & \text{for} \quad p^2 \le c_a^{-2} \\ \exp\left(-2\omega\sqrt{p^2 - c_a^{-2}}\,Z\right) & \text{for} \quad p^2 > c_a^{-2} \end{cases} \tag{A8}$$

Applying the inverse temporal Fourier transformation to equation (A8) yields equation (10) in the main text. Here the evanescent field (at $p^2 > c_a^{-2}$) has been neglected.

*This article was published online on 7 November 2012. Page extents were subsequently corrected in the references for Hunziker *et al.* (2012) and Wapenaar and Fokkema (2006).